

Citation

Vogel, Y. and Zhang, J. and Darwish, N. and Ciampi, S. 2018. Switching of Current Rectification Ratios within a Single Nanocrystal by Facet-Resolved Electrical Wiring. ACS Nano. 12 (8): pp. 8071–8080.
<http://doi.org/10.1021/acsnano.8b02934>

Switching of Current Rectification Ratios within a Single Nanocrystal by Facet-Resolved Electrical Wiring

Yan B. Vogel, Jinyang Zhang, Nadim Darwish and Simone Ciampi**

Department of Chemistry, Curtin Institute of Functional Molecules and Interfaces, Curtin University, Bentley, Western Australia 6102, Australia.

*Email: simone.ciampi@curtin.edu.au, nadim.darwish@curtin.edu.au.

ABSTRACT

Here we show that within a single polyhedral metal oxide nanoparticle a nanometer-scale lateral or vertical sliding of a small metal top contact (*e.g.* <50 nm) leads to a 10-fold change in current rectification ratios. Electron tunneling imaging and constant-force current–potential analysis in atomic force microscopy demonstrate that within an individual p-n rectifier (a Cu₂O nanocrystal on silicon) the degree of current asymmetry can be modulated predictably by a set of geometric considerations. We demonstrate the concept of a single nanoscale entity displaying an in-built range of discrete electrical signatures, and address fundamental questions in the direction of “landing” contacts in single-particle diodes. This concept is scalable to large 2D arrays, up to millimeters in size, with implications in the design and understanding of nanoparticle circuitry.

KEYWORDS: current rectification, nanodiode, tunneling AFM, electrical mapping, polyhedral nanocrystals growth, Cu₂O nanoparticles.

The symmetrical framework of crystals shapes has attracted our curiosity since the dawn of civilization,^{1,2} and beyond the immediate beauty apparent to the eye of the observer, chemists and engineers appreciate the deeper scientific value of crystals in the nanometer domain.³ The properties of a nanocrystal, from its chemical reactivity to its ability to either store or conduct charge, are linked to its shape, to the presence of edges between crystals faces or steps between atomic terraces.³⁻⁹ Rectification of electrical conductivity in semiconductors forms the basis of our digitized civilization and semiconducting crystal particles hold great promises in nanoscale electrical circuitry. To realize this potential in a real-world circuitry setting, and for instance to have multiple entities operating at the unison, the particle(s) has to be deposited on a sturdy surface and organized at interfaces. This introduces delicate aspects of contact structure, geometry or alloying between the particle and its support.^{10,11} In 2015 Huang and co-workers succeeded in forcing a direct current across a Cu₂O rhombicuboctahedron particle while holding it between two needle-shaped metal contacts. They found the particle can behave as a diode when connections are carefully made to its $\langle 110 \rangle$ and $\langle 111 \rangle$ faces, but more importantly, the rectifying properties of this single-entity system are almost completely lost when the electrical wires “land” instead on its $\langle 100 \rangle$ and $\langle 111 \rangle$ faces.⁴ This shows us glimpses of the extent to which the engineering of the electrical connections between a nanoparticle and its electrified supports are not innocent factors in a meaningful and reproducible charge transport measurement. It also establishes a conceptual path towards multiple electrical signatures, *e.g.* a switch of rectification ratios, being achieved within a single active component. Here we provide insights on this “contact landing” factor for single-particle circuitry that is supported on a macroscopic substrate, showing its magnitude and implications. We do this by means of high-resolution electrical mapping of rectifiers made by Cu₂O nanoparticles deposited on a silicon electrode, providing quantitative insights on factors such facet-/shape-dependent

rectification, role of inter-particle spacing on knee voltages and leakage currents, and show that facet-to-substrate obliquity is a powerful aspect defining the current response of a nanodiode. By first overcoming the hurdle of controlling particles shapes and densities within the same sample, without changes to additives, and with no use of organic capping agents nor templating, all of which could inevitably introduce electrical “artefacts”, we have explored a sub-micrometer electrical view within individual diodes of metal oxide particles arranged in large 2D micrometre- to millimeter-scale arrays.

RESULTS AND DISCUSSION

Array construction: opto-electrochemical control of particle shape and inter-particle spacing. Prior to proceeding to the high-resolution and high-bandwidth electrical mapping it was key to access experimentally simultaneous control on both particle shapes and distances. Further, multiple combinations of the two variables above had to be realized within the same macroscopic sample. The latter requirement, *i.e.* the concurrent control on spacing and shapes to be accessed within the same macroscopic support, is aimed at removing sample-to-sample variability to the largest extent possible, namely minimizing random fluctuations to series resistance, stray capacitance and density of surface states. The requirement of control on inter-diode spacing is to avoid or gauge proximal effects,^{12,13} which for instance are known to affect electro-catalytic properties of nanoparticles in arrays.¹⁴ The obvious possibility of an overlap between space-charges of nearby particles, coupled to lack of control on the spacing of these small rectifiers, may lead the experimentalist to draw erroneous conclusions on charge transport when the measurement has a sub-micrometer lateral resolution. As photo-electrochemical reactions involve only clean stimuli that can be addressed with high spatial and temporal control – voltages and light – amorphous silicon (a-Si thereafter) was employed as the light-responsive n-type semiconductor substrate onto which p-type Cu₂O nanoparticles¹⁵

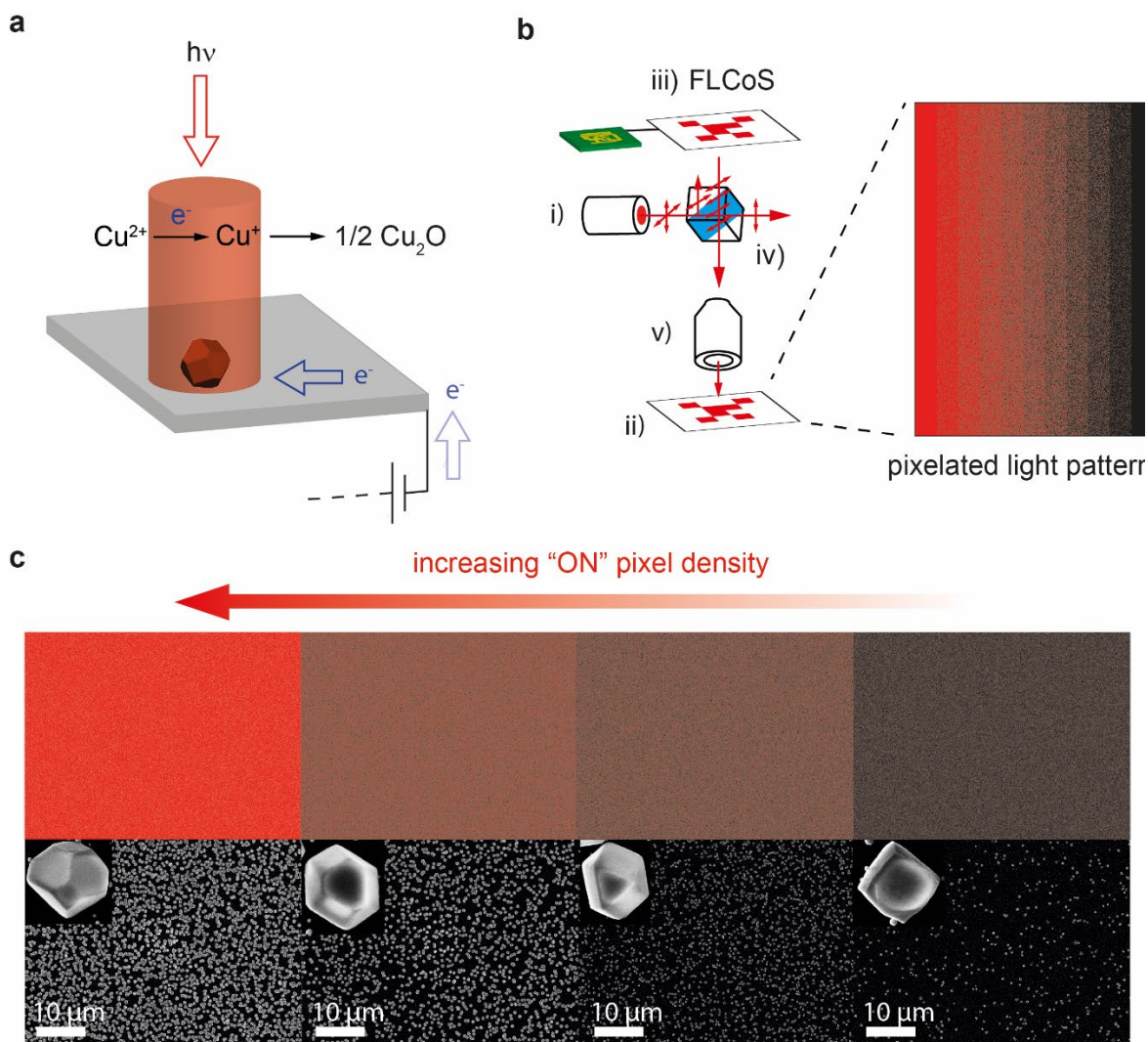


Figure 1. Opto-electrochemical guided synthesis of p-n arrays. (a) Schematic depiction of the light-addressable growth of Cu_2O particles arranged in microscale patterns at an amorphous silicon (a-Si) electrode surface. Cu_2O deposition follows the localized electrochemical reduction of cupric to cuprous ions from an electrolyte solution in contact with the illuminated a-Si photoelectrode. (b) Collimated and polarized light from a red LED (i) is projected onto a photoconductive a-Si working electrode (ii) after being selectively (2D) reflected by a ferroelectric liquid crystal on silicon (FLCoS) micro-mirror and optics that act as spatial light modulator (iii-v). In order to control both illumination intensities and patterns, hence particle gradients, shapes and 2D arrangement of diodes, each of the over 3.1 million discrete and adjacent FLCoS elements (2048×1536) are individually-addressed allowing to generate any arbitrary image from a user-defined bitmap pattern of “ON/OFF” pixels. (c, upper panels), High-magnification views of representative “pixelated” patterns projected on the biased a-Si electrode. The pixel “ON” density drops from left to right (90%, 50%, 40% and 20%). (c, lower panels), SEM images showing the evolution in spacing and shapes within arrays of Cu_2O particles that are generated when the FLCoS illumination density decrease in response to changes of “ON/OFF” gradients. This is linked to changes in the particle’s shape (shown as an insets, mechanistic details in Figure 3). The bias of the a-Si is 0.0 V (vs. reference) and metal discharge is halted after having passed a charge density of $32\ \text{mC}\cdot\text{cm}^{-2}$.

are electrodeposited. Spatially-confined red light (625 nm) is delivered on the a-Si working electrode *via* a spatial light modulator based on an array of individually-addressable

ferroelectric mirrors (*i.e.* “pixels” of ferroelectric liquid crystals on silicon, FLCoS, see Methods section). The projected light is used to excite the a-Si substrate and temporarily removing a kinetic barrier¹⁶ allowing the discharge of Cu^{2+} ions, hence localized Cu_2O deposition to build our model p-n junction. The electrode process where Cu^+ is hydrolyzed to form Cu_2O is generally accepted and schematically depicted in Figure 1a.^{15, 17} The image projected onto the wet side (silicon/electrolyte) of the a-Si electrode during copper discharge (Figure 1b and 1c) is made-up by an excess of 3.1 million “pixels” with a lateral resolution of 4.6 μm . Figure 1c shows that by adjusting the density of “ON” pixels along the x -direction it is possible to tune inter-particle distances. This aspect is most relevant towards setting conditions that are ideal for a direct test of the electrical characteristics of the diodes. Any user-defined change in the array, for instance as shown in Figure 1c by tuning densities and shapes of Cu_2O particle, is attained within a single macroscopic sample and without changes to additives or templating.

Available methods for organizing nanoparticles in 2D structures with control on spacing, most often rely on assembly guided by gradients of either grafted molecules or molecular weights.¹⁸⁻²⁴ In the current context a molecular gradient would introduce an additional barrier element, or a variable set of surface states, that would be hard to predict or account for in terms of electrical behavior. But even more importantly, all common templating methods do not allow for simultaneous control of both densities and shapes. From the data in Figure 1c it is however apparent that a change in density is linked to a change in the degree of “cubicity” of the particle (high-magnification SEM data shown as insets). The mechanism by which we linked photoelectrochemistry to polyhedral character is discussed further below, while in the following section we proceed first to explore the relationship between shapes and flow of dc currents within a single Cu_2O /a-Si entity.

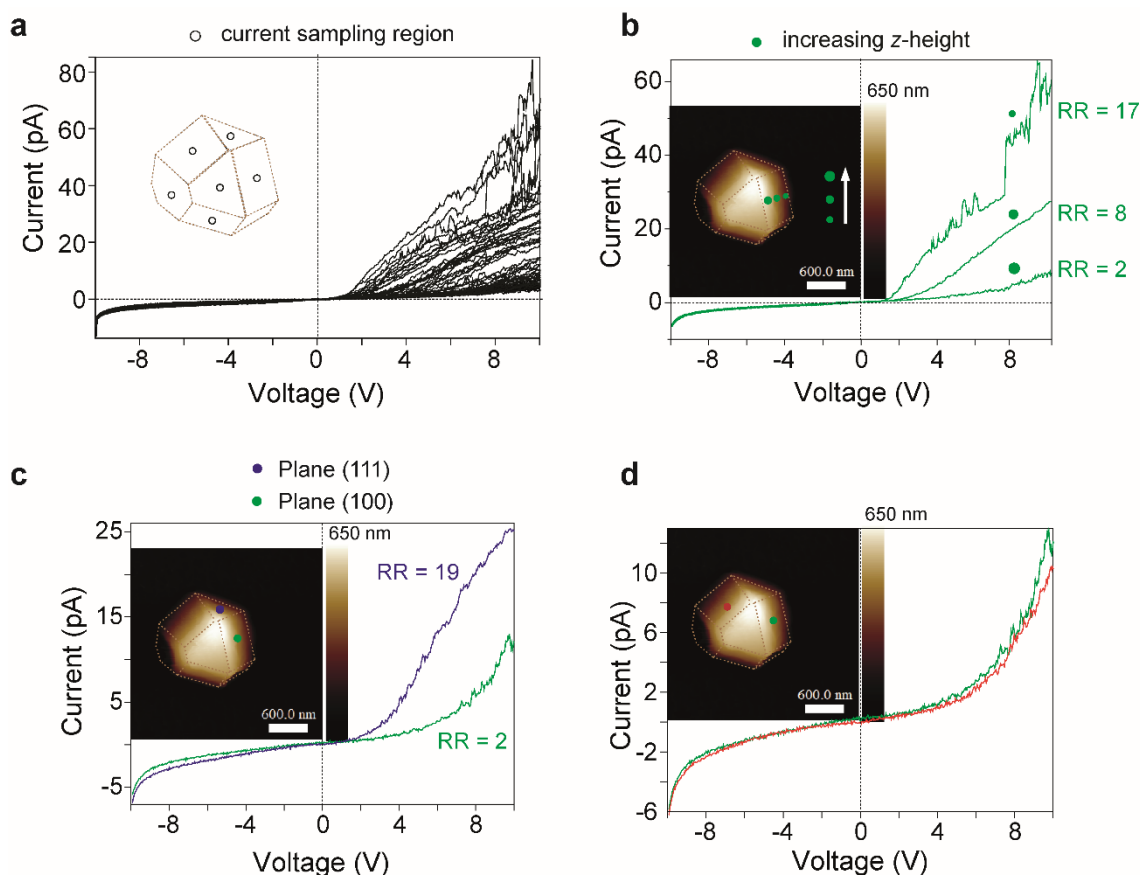


Figure 2. Electrical mapping of a single-particle polyhedral rectifier. (a) Dispersion of the current–potential spectra acquired by PeakForce tunneling AFM on all of the accessible faces of a p-type Cu_2O cuboctahedron grown on n-type silicon. The vertical z -height of the AFM tip contact away from the junction with the a-Si substrate was varied in the measurements over the range 100–600 nm. (b) Current–potential curves sampled across the same $\langle 100 \rangle$ facet as a function of changes to the contact z -height. The exact sampling location is indicated with ● symbols in the height AFM micrograph (z -heights of 100 nm, 200 nm and 400 nm). (c) Current–potential curves comparing rectification characteristic at the same vertical distance from the p-n junction (350 nm) but on either $\langle 100 \rangle$ or $\langle 111 \rangle$ planes (green vs blue traces). (d) Current traces at the same z -height (350 nm) but on separate $\langle 100 \rangle$ facets. Rectification ratios (RR) are given at ± 8 V. Cu_2O particles were electrodeposited at a bias of 0.1 V under electrode illumination (1030 lx) by transferring a total charge density of $32 \text{ mC}\cdot\text{cm}^{-2}$. Forward currents of the junctions, *i.e.* when Cu_2O particles are biased positive with respect to the silicon substrate, are in the positive quadrant.

Making electrical contacts to a polyhedral particle. Figure 2a shows current–potential spectra (I–Vs hereafter) performed on precisely-selected locations over a single polyhedral particle; to begin with a Cu_2O cuboctahedron consisting exclusively of $\langle 100 \rangle$ and $\langle 111 \rangle$ faces. As expected based on material-specific band diagrams (Supporting Information, Figure S1),²⁵ this junction is highly rectifying and it shows an exponential increase in current only when the

negative voltage is applied to the n-type silicon substrate and the positive to the p-type Cu₂O nanoparticle. When the polarity is inverted the junction is forced into reverse bias, with only a small diode leakage current that is independent of voltage within a reasonably large window. It is also evident from the I–Vs shown in Figure 2a that the electrical behaviour of a single particle is a strong and complex function of the exact positioning of the contact made by the platinum AFM tip. For instance, I–Vs taken at constant force within the same facet and increasing z-heights of the AFM contact away from the Cu₂O/silicon junction show a progressive attenuation of the forward current (Figure 2b). The apparent shift in the knee voltage and the 8-fold decrease in rectification observed within the same particle is therefore most likely a reflection of an increased length of the resistive path and not due to changes in the built-in electric field of the junction (*vide infra*). Huang and co-workers have suggested that a longer distance separating two electrical contacts in a nanoparticle can reduce significantly the measured current.⁴ This is key, as it shows that in a nanoscale diode even a minor (<200 nm) x-direction movement of the point where the electrical contact lands over a tilted facet (z-displacement between 100 and 400 nm) will have a dramatic consequence in the electrical response even when the p-n interface is itself unperturbed. From the data in Figure 2b it is apparent that at this scale and resolution the analysis on charge transport is meaningful only after having accurately and precisely controlled the contact height. This aspect becomes of immediate importance when, for instance, attempting a comparison between the electrical behaviour of different facets within the same entity (Figure 2c) or between particles of different sizes (*vide infra*, Figure 5). The simplest hypothesis is that of a link between series resistance and a decrease in the slope of the forward current (see Figure S2a). This is supported by the data in Figure 2c where we show the difference between two I–Vs that are taken at the same z-height but moving between <100> and <111> facets. The rectification ratio is 10-fold larger when the contact lands on the <111> face, which is likely to be a consequence of the lower

conductivity of the $\langle 100 \rangle$ face in Cu_2O , with analogies to the facet-dependent conductivity of other semiconductors (see band diagram in Supporting Information, Figure S1).^{3,4, 26-28} The poorer conductivity and photocatalytic activity of the $\langle 100 \rangle$ face has been previously explained as a higher energy barrier for holes conduction from the bulk Cu_2O material to the surface.^{4, 29} Our high-resolution electrical AFM mapping points therefore to the conclusion that for a single nanoscale polyhedral/macroscopic substrate entity the current–voltage characteristics will become indistinguishable and reproducible only if care is taken to make top contacts on facets having the same orientation and precisely locating these contacts at the same height away from the junction with the substrate. Figure 2d shows this by probing separate $\langle 100 \rangle$ facets at the same z-height offset and indeed the two electrical signatures are now superimposable.

Degree of Cu_2O cubicity and electrochemical potential. The high-resolution AFM electrical data discussed in the previous section highlights the complex and heterogeneous electrical landscape within a single a Cu_2O cuboctahedron. These measurements allow us to draw preliminary conclusions on charge transport in respect to facet-dependent rectification, displacement of the contact away from the p-n junction and complexity introduced by the obliquity of individual faces. As shown in both Figure 1c and Figure 3a, the clean light stimulus that guides the discharge of cupric ions and influences inter-particle spacing is also linked to a progressive increase in “cubicity”. We therefore attempted to gain a correct and satisfactory understanding of the electrochemical factors at play, for instance enabling us to address independently, and *at will*, either inter-particle spacing or shapes, and as stressed above, all with no requirement of templating. The observed trend in the increase of inter-particle distances under a dimmer light can be understood as a decrease on the number of sites on the photoconductor with sufficiently fast kinetics for nucleation.³⁰⁻³² The trends on Cu_2O particle “cubicities” are however much less obvious. An instructive starting point is that an equivalent

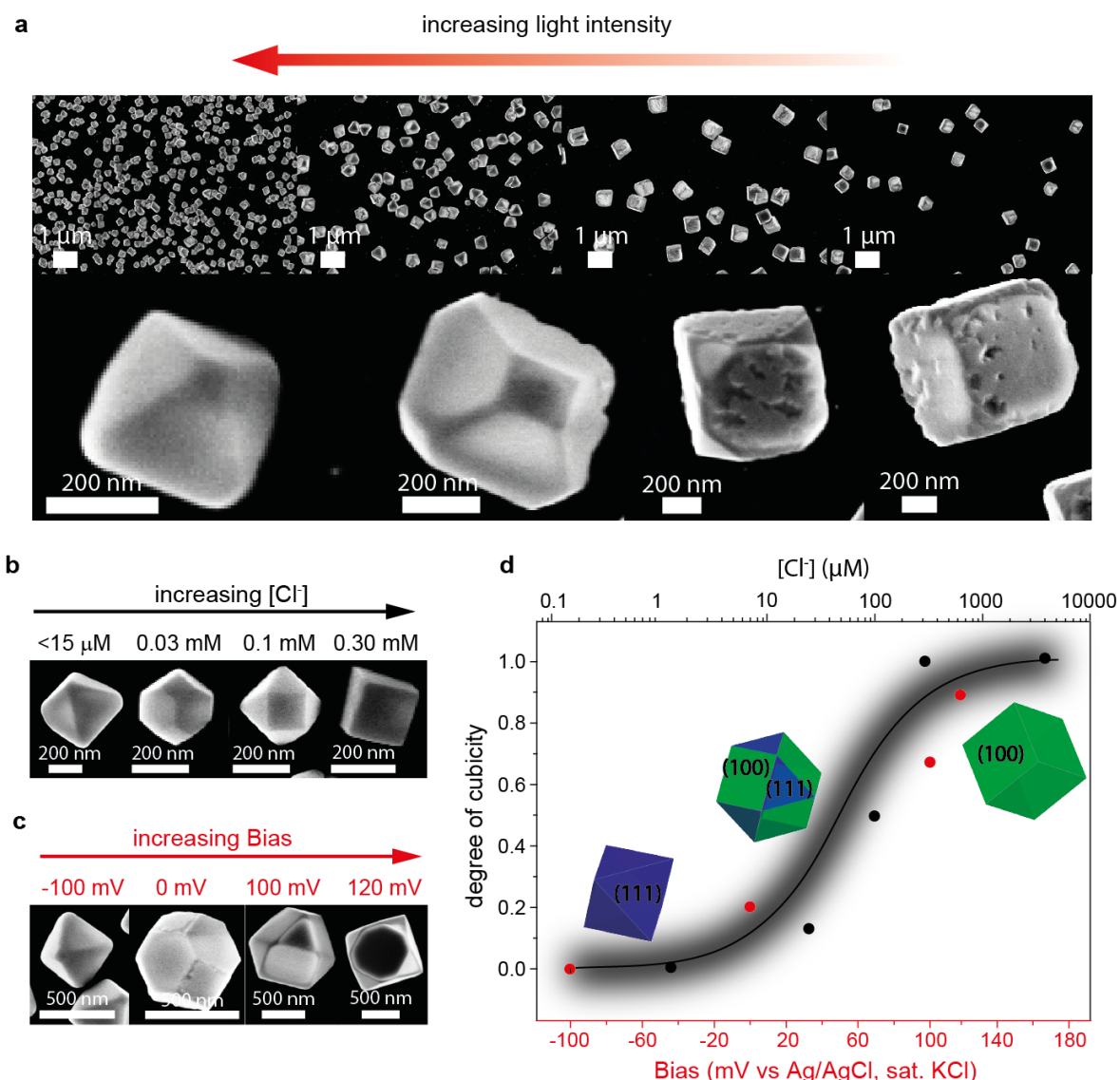


Figure 3. The “degree of cubicity” for cuprous oxide particles is a function of both surface potential and bulk concentration of halide ions. (a) SEM images for Cu_2O particles electrodeposited at a fixed bias (-0.10 V) and constant Cl^- bulk concentration (< 15 μM , determined by conductivity after ion chromatography separation using a Dionex DX-500 system) under variable electrode illumination (1030 lx, 390 lx, 240 lx and 170 lx, from left to right). (b) Shape evolution at a constant electrolysis potential (0.10 V) upon a progressive increase of Cl^- bulk concentration. (c) Shape evolution in response to a progressive anodic bias (from left to right, bias increased from -0.10 V to 0.12 V) and in the presence of < 15 μM of Cl^- . (d) Plots of the “degree of cubicity” versus bias (or versus concentration, top x-axis) under constant illumination (1030 lx) based on a putative Langmuir isotherm (solid line). The solid points in (d) reflect surface area considerations based on SEM data in panels (b) (black points) and (c) (red points). The total transferred charge was kept constant at 32 $\text{mC}\cdot\text{cm}^{-2}$.

trend to that observed for the data in either Figure 1c (changes to the density of bright “ON” pixels) or in Figure 3a (changes to overall the LED power) is found for deliberate changes to the amount of chloride ions present in the electrolyte compartment (Figure 3b). We therefore

reasoned that changes in shapes associated with density changes could have two origins: a change in composition of the crystal being formed³³ or a surface energy effect linked to anisotropic adsorption of ions present in solution. XPS experiments dismissed changes in crystal compositions (Supporting Information, Figures S3 and S4), leaving open the second hypothesis. It is known that changes to the bulk concentration of chloride ions can guide the growth of copper and copper oxides crystals shapes, with the equilibrium shape being determined by the adsorption thermodynamics of the halide on the planes with slower growth rates, nominally the $\langle 100 \rangle$ and $\langle 111 \rangle$ planes.^{33,34} For the case of copper crystals, the adsorption of bulk chloride ions can lower the surface free energy of the $\langle 100 \rangle$ significantly, with an excess of the anion leading to the exclusive formation of cubic-shaped particles.^{17, 34} An anodic process is involved in the adsorption of chloride on Cu_2O and this is likely to explain the trends in both Figure 1c and Figure 3a, showing a progressive transition from octahedral to cubic particles that tracks the decrease in particle density obtained via a dimmer substrate illumination. Lower amounts of Cu_2O results in higher chloride surface coverages, *i.e.* an increased $\text{Cl}^-/\text{Cu}_2\text{O}$ ratio from left to right panels in Figure 1c and Figure 3a, and hence a decrease in absolute value of the chloride chemical potential. As a further and more direct test, Figure 3b shows the progressive transition from octahedral to cubic shapes when the concentration of bulk Cl^- is deliberately increased.

In electrodeposition the applied bias becomes a further “knob” on chemical potential (now electrochemical potential). The bias control on Cu_2O “cubicity” is evident and it is shown in Figure 3c. It removes the need of tuning shapes by changes in composition of the electrolysis mixture. When the concentration of bulk chloride ions is fixed, a bias-driven change to the chemical potential of halide translates into the octahedron-to-cube transition. Both the electrochemical potential and the chloride concentration are therefore critical and synergic parameters in determining the stabilization of the Cu_2O $\langle 100 \rangle$, hence the particle morphology.

This aspect of Cu₂O crystal growth is virtually unexplored and it is crucial here as it removes the need of tuning shapes by changes in the composition of the electrolysis mixture. It was anticipated by a theoretical paper published by Bonnet and Marzari in 2013,³⁵ predicting that the “degree of cubicity” of platinum particles is governed by electro-adsorption of hydrogen that follows an isotherm-type graph.³⁵ The plot in Figure 3d for the experimental “degree of cubicity” vs the applied bias (with chloride concentrations in the top x-axis) suggests indeed a parallel between our and the above Pt/H system; the plot shows that changing the bias by a factor $2.3 RT/F$ (*ca.* 59 mV at 25° C) has a similar effect on the equilibrium particle shape as an order of magnitude change to the bulk Cl⁻ concentration. However, we remark that the transition from octahedrons to cubes is only accessible by electrochemical “clean” means when the potential required to discharge the metal ion is positioned in proximity of the raising part of the curve in Figure 3d. Due to the “steep” sigmoid nature of the putative adsorption isotherm curve, the practical challenge rests on ensuring that the “rising” position of the curve is centred on an accessible bias window. The curve can be shifted for instance by changes to potential or by changing the concentration of Cl⁻; by increasing the Cl⁻ concentration the shift is towards the negative bias and the cube-to-octahedron transition appears therefore at more cathodic potentials (Figure S5). In fact, if the potential is stepped more cathodic the transition to cubes begins at lower densities (Figure S6). The applied potential needs however to remain cathodic of the apparent formal potential in order to be able to reduce the copper ions at a practical rate (*e.g.* no deposition occurred at potentials above *ca.* 0.15 V). We note that higher concentration of Cl⁻ (0.3 mM or above, see Figure S7) the particle’s shape becomes potential-independent as the system is now positioned on the right side of the isotherm where the surface excess of halide does not change with bias.

Nanocrystal obliquity effect on charge transport at fixed contact area and inter-particle spacing. The previous two sections highlight the broadness of the electrical landscape within

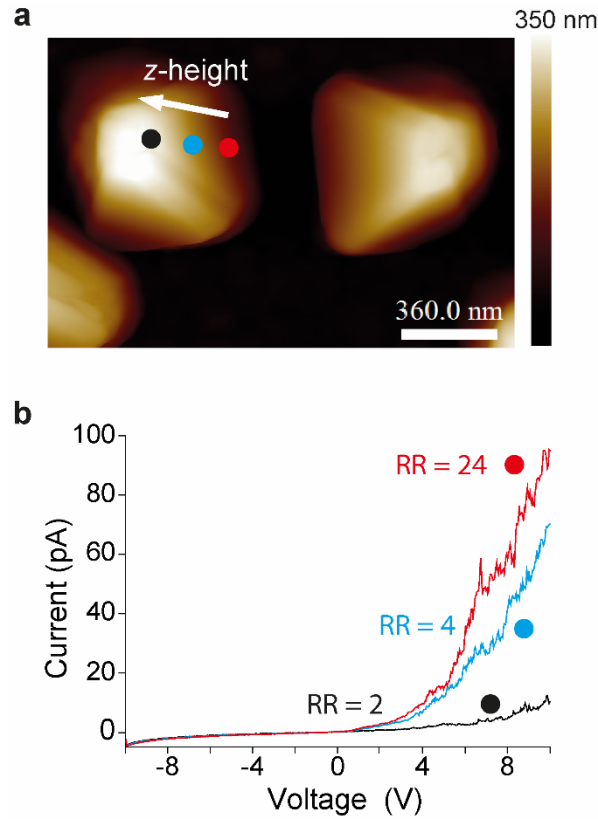


Figure 4. Current-potential curves at different heights of a single octahedral Cu_2O nanocrystal exposing only $\langle 111 \rangle$ facets. (a) AFM height image with solid dots symbols representing the region on the height image where the diode currents are sampled. (b) Current-potential curves as a function of the z-height away from the silicon surface. The I–V sampling location is indicated with ●, ● and ● symbols (z-height of 70 nm, 150 nm and 300 nm, respectively). The particles were electrodeposited at -0.1 V under electrode illumination (1030 lx) and until reaching a transferred charge density of $32 \text{ mC} \cdot \text{cm}^{-2}$.

a single polyhedral Cu_2O /silicon rectifier and describe the principles to control geometries and densities on a scalable platform. Figure 2 points visually to the importance of controlling the geometry of the p-component as I–V spectra turned out to be highly dependent on the current sampling location; asymmetry in the p–n behaviour depends strongly on face indexes and obliquity with no requirement to have changes made to the p–n junction itself (*i.e.* changes in bands alignments, tuning work functions or changes to surface states). We have in the first section advanced the hypothesis that for a junction made of a Cu_2O cuboctahedral particle (Figure 2b) a *ca.* 8-fold change in rectification is a direct manifestation of a change in series resistance upon a vertical displacement of the contact made by the AFM tip on a tilted $\langle 100 \rangle$ face. A direct proof of this putative contact height dependency would be strengthened by the

analysis of a single-faceted nanocrystal. An octahedral particle is a perfect model system as it exposes only $\langle 111 \rangle$ faces with a single tilt with respect to the n-type substrate (Figure 4a). The analysis shown in Figure 4b is done within a single octahedral Cu_2O particle allowing for a straightforward change on the height at which the top contact is made, ruling out to a large degree that changes to built-in potentials are due to differences on bottom contact or neighbouring effects. As shown in Figure 4b the rectification tracks the height of the contact; the reverse leakage current remains practically unchanged while the slope of forward current increases significantly with decreasing distances between contact and a-Si substrate.

Adjusting junction areas and particle densities. Octahedral and cuboctahedral particles offer great insights on charge transport by facets-related and contact landing effects, but they do this at the expense of a poorer control on the area of the p-n junction. For example, geometrical considerations on the representative AFM height data in Figure 4a suggest that the Cu_2O particle has grown either as a truncated or cut octahedron. As a result of this, any attempt of a rigorous comparison between current densities on different particles across the array – for instance to assess diagnostic parameters such as the magnitude of minority carriers currents in reverse bias or changes to the built-in potentials of the junctions by gauging knee voltages in forward bias – would be not possible. On the other hand, cubic Cu_2O particles present only $\langle 100 \rangle$ faces at orthogonal angles, making it difficult for the cube not to sit uniformly on a single face. This assumption can be further validated by SEM analysis (Figures S8 and S9) and even more rigorously by height measurements in AFM (Figure 5a-c). This aspect also becomes important when making arrays of several thousand of nano-rectifiers that should perform homogeneously with controllable and reproducible electrical properties. From the data in Figure 5d-i (Figure 5d-f show AFM tunneling current images taken at a constant force on the Cu_2O cubes with the substrate biased at 2 V) it is apparent that with negative voltages on the n-type a-Si there is an apparent inverse relationship between current densities and cube heights

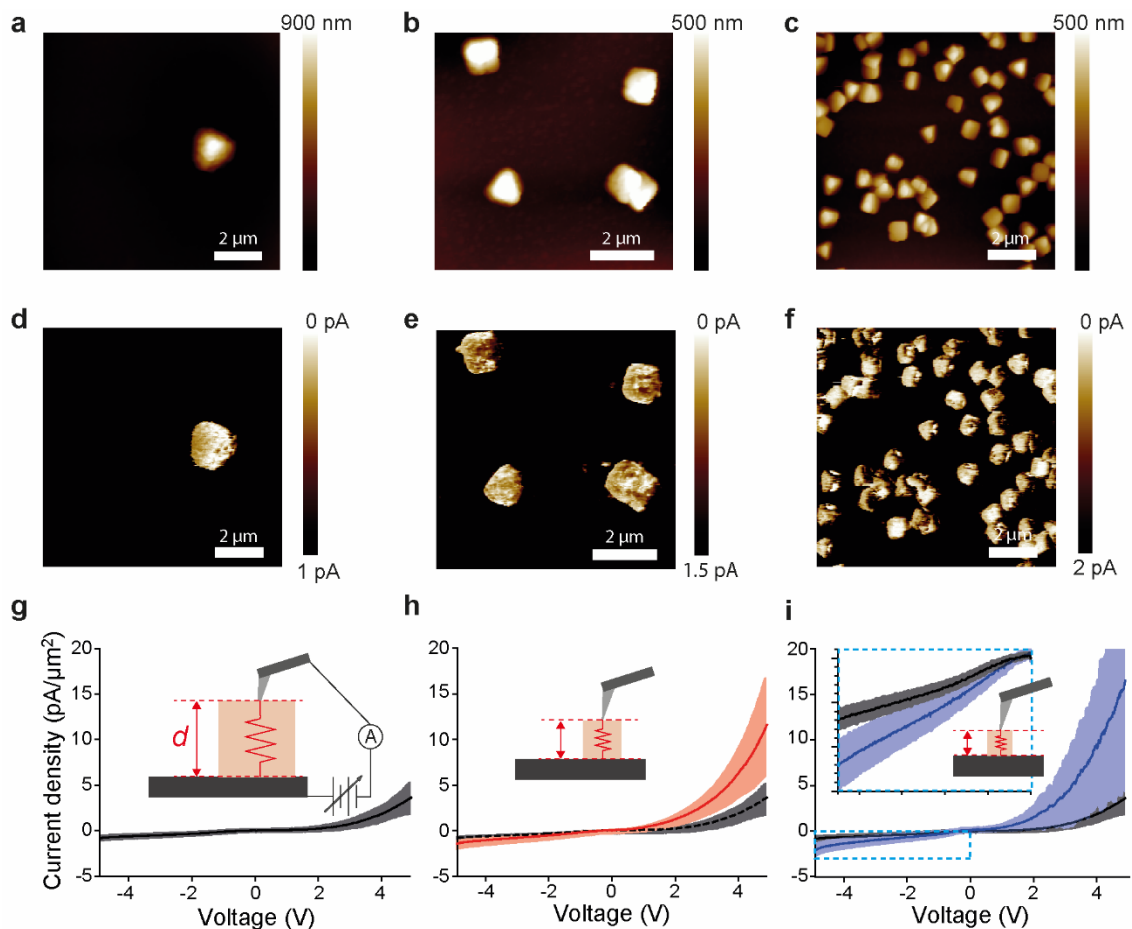


Figure 5. Size-dependent degree of rectification for Cu_2O cubic crystals. (a-i) AFM data (height micrographs in (a-c), tunneling current images taken at 2 V in (d-f) and current density–potential curves in (g-i)) for Cu_2O cubes of face area of $4.0 \mu\text{m}^2$ (a, d and g), $1.7 \mu\text{m}^2$ (b, e and h) and $0.7 \mu\text{m}^2$ (c, f and i) and average heights (d) of 852 nm (a, d and g), 474 nm (b, e and h) and 313 nm (c, f and i). The experimental rectification ratio (RR) increases from 4.5 to 8.1 when d decreases from (g) to (i). The current–potential plots represent an average of 20-50 curves that were sampled at a constant force and at different locations on exposed top-faces, with the standard deviation shown as semi-transparent colored contours. RR are taken at ± 4.5 V. The particles were electrodeposited at -0.1 V, setting a charge limit of $32 \text{ mC}\cdot\text{cm}^{-2}$ and by projecting a discrete gradient of “ON” (bright) pixels across a single silicon photoelectrode (Figure S17a, Supporting Information). The density of “ON” pixels was 20% (a, d and g), 30% (b, e and h) and 40% (c, f and i). Tunneling current images with an inverted-current scale are shown in Figure S10, SEM images for this sample are shown in Figure S9 and individual representative current–potential traces are shown in Figure S11.

(Figure 5g-i), indicating once more that the length of the current path across the Cu_2O particle is still a dominant parameter in the forward direction. In the reverse bias the expected trend would be one somehow resembling the findings for a contact sliding down a tilted octahedral face (Figure 4). However, unlike the octahedral system, the magnitude of the reverse current density moves towards resistive as the z-height of the top contact gets smaller (Figure 5i). Dark junction currents in reverse bias are the manifestation of thermal minority carriers generated in

proximity of the space-charge layer, in other words at a given temperature the current in this regime should scale with area only. The AFM current analysis in Figure 5 is performed within the same sample, during the same session, and currents are normalized by area. The progressive increase in reverse current could be due to a heterogeneous a-Si substrate, especially considering the well-documented irreversible photo-induced changes for a-Si,³⁶ but this possibility was discarded since no changes are observed in the reverse current of I–V spectra taken on the same sample but off the particles, *i.e.* on the a-Si substrate (Figure S13). Considering that the increase in reverse current seems to be paralleled by a decrease in built-in potentials (Figure 5i), there is the possibility of an increase in density of surface states that manifests as an increased in shunt (parallel) resistance at high particles densities.

Interestingly, this is opposite to the initial expectation of space-charges extending along the lateral direction in silicon leading to an overlap between depletion layers of nearby particles.^{12,13} This overlap would slow down the onset of the forward current, instead of favoring as it is experimentally observed for the small particles/high density samples (Figure 5i). Further, the apparent drop in built-in potential is analogous to that observed within a single octahedron (Figure 4) hence unlikely to be a mere consequence of defects/surface states. To gain insights on this we used the FLCoS projector to prepare arrays of Cu₂O cubes of the same size but at either short or large inter-particle distances (*ca.* two or five times the particle width, Figure 6a-b. SEM data in Figure S14). This is to rule out that a poorer ideality factor for the smaller diodes arises from a change in the bottom contact that is linked to the particle size.³⁷ The current-potential curves in Figure 6c don't show any statistically significant difference in the forward bias, which is practically unchanged with changes to the inter-particle distance. This is indicative of the built-in electric field inside the Cu₂O crystal being independent of spacing, and the onset of forward currents being therefore a stronger function of the particle series resistance (*e.g.* Figures 4 and 5). The much larger resistivity of Cu₂O relative to a-Si may

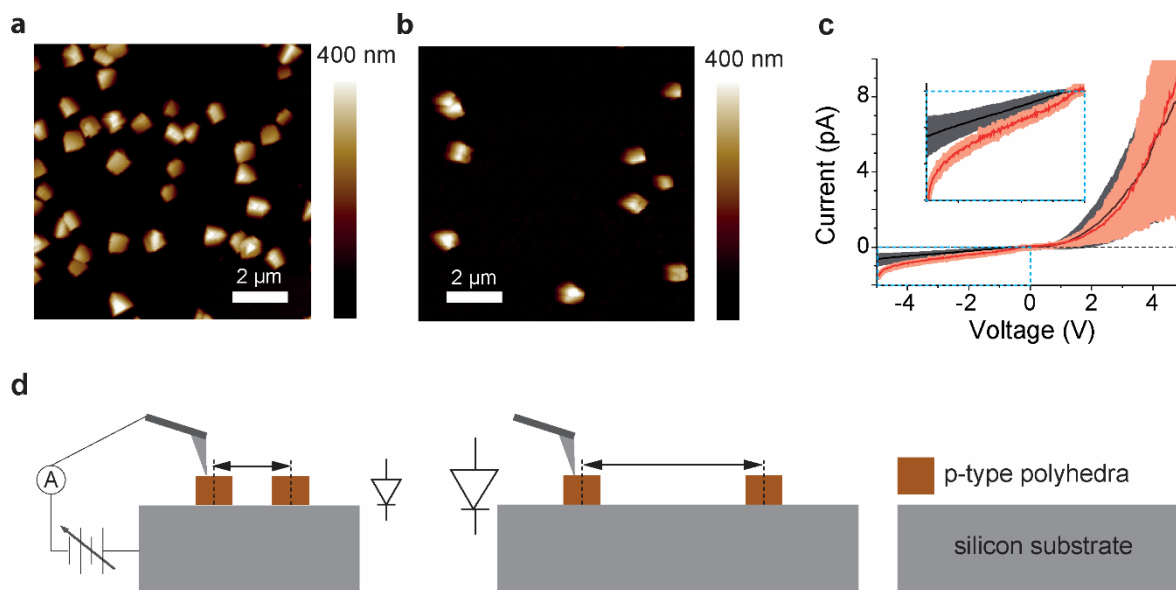


Figure 6. Current-potential relationship of cubic Cu_2O crystals as a function of the array inter-particle distance. (a-b) AFM height images of cubic particles of similar size (average cube width of 800 nm) and inter-particle distance of *ca.* 1.5 μm (twice the particle width) and 4 μm (5 times the width), respectively. (c) Comparison of the current-potential relationship as a function of the inter-particle distance. The red line is for densely-packed particles and the black line is for the low density system, panels (a) and (b) respectively. The solid lines represent the average of 50 independent I–V spectra taken on different locations of isolated particles and the standard deviation is shown as a semi-transparent contour plot. (d) Schematic depiction of the electrical connection and of the changes in the average particle spacing-to-particle widths for data in panels (a) and (b). Rectification ratios (RR) are calculated for -4.5 to 4.5 V and are $\text{RR} = 8.5$ and $\text{RR} = 13$ for particles of panel (a) and (b) respectively. Particles were electrodeposited at 0.0 V and using a 40% pixel density and $16 \text{ mC}\cdot\text{cm}^{-2}$ in (a), and a 20% pixel density and $3.6 \text{ mC}\cdot\text{cm}^{-2}$ in (b) (see Figure S17b for details on the illumination patterns). Representative individual current–potential curves for the data presented in panel (c) are shown in Figure S12.

result in the former contributing in larger measure to the depletion region of the p-n junction. This is supported by I–Vs spectra that are acquired on the a-Si substrate as a function of changes to inter-particle spacing (Figure S13). Here, unlike for measurements taken precisely on the Cu_2O particles (Figure 6), I–V curves on silicon show a slightly slower onset for the forward current when taken in densely-packed areas, suggesting therefore a 2D change to the degree of space-charge overlap. Notably the reverse bias blocking properties of the smaller cubic rectifiers are progressively restored as the inter-particle distance are further increased (Figure 6c). Lower reverse bias leakage currents, hence a better conformity to pure thermionic emission is unrelated to particle size, but more so to distances between closest neighbors. This is further confirmed by control experiments where the nanoparticle size is changed while the particle density is kept constant, showing no apparent changes to the leakage current (Figure S15).

CONCLUSIONS

In this work we have unveiled links between electrical rectification and specific sets of polyhedral geometries, obliquity of crystal facets and nanoparticle dimensions. We have shown that it is possible to use a combination of clean stimuli – light and bias – to modulate the anisotropic interactions between charged ions and surfaces, in turn predictably linking near-surface electric fields to the equilibrium shape of a Cu_2O nanocrystal. This has enabled us to tune the spacing and the polyhedral shape of Cu_2O particles on silicon electrodes. This aspect of the work is also expected to have implications beyond electrochemistry, for instance aiding the emerging research area of electrostatic catalysis of reactions.³⁸ Further, the fine control and predictive power we show here for Cu_2O particles is a scenario that can be extended to the synthesis of other materials. For example, hydrogen is known to adsorb preferentially on the $\text{Pt}\langle 100 \rangle$ face and electrostatic could be the cause behind the unexplained high “cubicity” reported for particles growing when hydrogen permeates towards the cathode across fuel cells membranes.³⁹ Using high-resolution electrical surface probe measurements we have demonstrated that a range of electrical signatures co-exist within a single-particle rectifier, a finding that is of immediate relevance when choosing the position and accuracy for the “landing” of electrical contacts in single-particle circuitry. For instance, a one order of magnitude facet-dependent change in current rectification is the result of wiring a top contact on either the $\langle 111 \rangle$ or $\langle 100 \rangle$ neighbouring facets of a cuboctahedral Cu_2O particle. Changes in the current asymmetry of similar magnitude are also observed after a minor, nanometer-scale, sliding of the contact within a given $\langle 111 \rangle$ facet of an octahedral particle. The latter is a consequence of a tilt of the facet away from a parallel alignment with the p-n junction. A similar dispersion in the electrical signatures arises also for changes in the size of Cu_2O cubes that expose only $\langle 100 \rangle$ planes that are found in perfect alignment with the junction. Within an individual single nanocrystal the landing of the conductive wiring governs the device electrical

performance, it will be a friend or a foe in nanoparticle circuitry and these findings assist in the design, scale-up and understanding of these connectors. It can also be envisioned that these observations of facet-dependent changes in dc conductivity can translate into a handle to enable 2D resolution of chemical kinetics within a single micro-/nano-particle. For example, it could become a viable mean to address chemical reactivity (coupled to the flow of currents) to a discrete location within a single particle; such as facet-resolved grafting of aryldiazonium salts,⁴⁰ defining vertical or lateral chemical gradients by the reductive desorption/oxidative re-deposition of sulfur-containing molecules⁴¹ or a localized polymer growth.

EXPERIMENTAL SECTION

Materials. Unless noted otherwise all chemicals were of analytical grade and used as received. Ammonium sulphite (92%), 1,8-Nonadiyne (98%), sulfuric acid (H_2SO_4 , PURANAL, 98%), hydrogen peroxide (H_2O_2 , MOS PURANAL, 30%) were obtained from Sigma Aldrich. Ultra-high purity Argon gas was obtained from BOC. Copper sulphate (CuSO_4 , 99.5%) was from Chem-Supply. Potassium sulphate (K_2SO_4 , 99%) and potassium chloride (KCl , 99.8%) were from Ajax Finichem. Redistilled solvents and Milli-Q water ($>18 \text{ M}\Omega \text{ cm}$) were used for substrate cleaning, surface modification procedures and to prepare electrolytic solutions. Deposition of a 1 μm -thick layer of amorphous silicon (a-Si) on prime grade 100-oriented ($\langle 100 \rangle \pm 0.5^\circ$) silicon wafers (Siltronix, S.A.S, Archamps, France) was performed following a previously reported procedure.³⁰ The a-Si coated wafers were cut into $1 \times 1 \text{ cm}$ pieces, cleaned with dichloromethane and water, immersed in piranha solution (100 $^\circ\text{C}$, 3:1 (v/v) mixture of concentrated sulfuric acid and 30% hydrogen peroxide), rinsed thoroughly with Milli-Q water, etched for 10 min in aqueous ammonium fluoride solution (degassed by bubbling with argon gas for 20 min in the presence of a small amount of ammonium sulfite),

rinsed sequentially with Milli-Q water and dichloromethane, dried under a nitrogen stream and placed on a glass sheet before dropping a small sample of 1,8-nonadiyne (*ca.* 50 μL) on the wafer. Reproducibility of the current-potential data was linked to the presence of a carbonaceous monolayer on the a-Si electrode. UV-assisted grafting of 1,8-nonadiyne followed minor modifications of a previously-reported thermal procedure.⁴² To limit evaporation of the diyne the liquid sample was top-contacted with a quartz slide. The samples were kept under positive nitrogen pressure and under UV light for 2 h (Vilber, VL-215.M, $\lambda = 312$ nm, nominal power output of 30 W and positioned approx. 200 mm away from the silicon sample). The chemically-passivated a-Si samples were then rinsed several times with dichloromethane, rested for 12 h in a sealed vial under dichloromethane at +4 °C and blown dry under nitrogen before being used as working electrodes in the electro-grafting of Cu_2O particles.

Assembly of the heterojunction. Cu_2O nanocrystals were deposited onto a-Si substrates ($10^4 \Omega\cdot\text{cm}$) by electrodeposition from an aqueous solution containing 0.5 M K_2SO_4 , 50 mM CuSO_4 and the indicated amount of KCl in a three-electrode PTFE cell (Figure S16) with an $\text{Ag}|\text{AgCl}|\text{Sat. KCl}$ reference electrode (all biases are specified against this reference electrode) and an FTO glass slide ($8 \Omega \text{ sq}^{-1}$, Solaronix SA, Switzerland) counter electrode. The geometric area of the working electrode was 0.28 cm^2 as defined by a circular Viton gasket. To ensure ohmic contact, indium-gallium eutectic was rubbed against the backside of the silicon electrode and pressed against a copper plate. A collimated light beam ($\lambda = 625$ nm, 710 mW (M470L3, Thorlabs) was shined on the “wet” side of the working electrode through the FTO glass counter electrode. The light source was spatially confined with micrometre resolution on the working electrode using a ferroelectric liquid crystal on silicon microdisplay (QXGA-3DM, Forth Dimension Displays).⁴³ The projected images were uploaded to the microdisplay printed circuit board memory as bitmap files generated using MATLAB®. The images at different “ON” pixel density were generated by a defined total number of “ON”

pixels of a certain area by a pseudorandom location of the “ON” pixels in the image. The pixel density of a specific area is defined as the number of “ON” pixels divided by the total number of pixels in that area. The system allows to modulate the intensity of the projected light by changing the LED forward current.

Atomic force microscopy. Sample topographies and dc conductivities were imaged with a Bruker Dimension Icon atomic force microscope. Data were obtained in air at room temperature and using conductive platinum tips (Rocky Mountain Nanotechnology AFM probes, 25Pt300B, with spring constant of 18 N m^{-1}). The imaging resolution was set to 512 points/line, the scan rate to 0.5 Hz and the peak force set to 20 nN. The Bruker PeakForce Tunneling AFM (PF-TUNA) module was used to acquire the I–V curves and conductive images. The I–V curves were taken at voltage sweep rates between 10 and 1 V/s, with a current gain of 20 pA/V and with the feedback being switched to contact mode with the deflection set-point kept constant to 2.25 μN . The bias routing is from the substrate to the AFM tip (the tip is grounded) and in the figures and text we adopted a convention on signs such that forward currents of our junctions are appearing in the positive quadrant (positive current, positive bias).

Scanning electron microscopy. The scanning electron microscopy (SEM) images were obtained using a Zeiss Neon 40EsB FESEM equipped with a Schottky field emission gun operating at 5 kV and a chamber pressure of approximately 4×10^{-6} mbar and a Tescan Mira3 FESEM, also equipped with a Schottky field emission gun operating at 5 kV, and a chamber pressure of 3×10^{-4} mbar. The “degree of cubicity” is defined as the ratio of $\langle 100 \rangle$ facets over the total nanoparticle surface area³⁵ and was estimated from the SEM images.

ASSOCIATED CONTENT

Supporting Information

The Supporting Information is available free of charge via the Internet at <http://pubs.acs.org>. Additional SEM images, AFM and XPS data, BMP files of FLCoS patterns, detailed discussion of the electrochemical mechanisms and data, instrumental schemes.

ACKNOWLEDGMENTS

This work was supported by grants from the Australian Research Council (ARC, DE160100732 (S.C.) and DE160101101 (N.D.)). We thank Dr. Jean-Pierre Veder from the John de Laeter Centre for the assistance with XPS measurements and Dr. Vinicius R. Gonçalves (School of Chemistry, The University of New South Wales) for the preparation of the a-Si layer. The authors acknowledge the use of Curtin University's Microscopy & Microanalysis Facility, whose instrumentation has been partially funded by the University, State and Commonwealth Governments.

REFERENCES

1. Lloyd, D. R., How Old Are the Platonic Solids? *BSHM Bulletin* **2012**, *27*, 131–140.
2. Paquette, L. A., Dodecahedrane—The Chemical Transliteration of Plato's Universe (A Review). *Proc. Natl. Acad. Sci. U. S. A.* **1982**, *79*, 4495–4500.
3. Huang, M. H.; Naresh, G.; Chen, H.-S., Facet-Dependent Electrical, Photocatalytic, and Optical Properties of Semiconductor Crystals and Their Implications for Applications. *ACS Appl. Mater. Interfaces* **2018**, *10*, 4–15.
4. Tan, C.-S.; Hsu, S.-C.; Ke, W.-H.; Chen, L.-J.; Huang, M. H., Facet-Dependent Electrical Conductivity Properties of Cu₂O Crystals. *Nano Lett.* **2015**, *15*, 2155–2160.
5. Kuo, C.-H.; Huang, M. H., Morphologically Controlled Synthesis of Cu₂O Nanocrystals and their Properties. *Nano Today* **2010**, *5*, 106–116.
6. Cheong, S.; Watt, J. D.; Tilley, R. D., Shape Control of Platinum and Palladium Nanoparticles for Catalysis. *Nanoscale* **2010**, *2*, 2045–2053.
7. Gao, D.; Zegkinoglou, I.; Divins, N. J.; Scholten, F.; Sinev, I.; Grosse, P.; Roldan Cuenya, B., Plasma-Activated Copper Nanocube Catalysts for Efficient Carbon Dioxide Electroreduction to Hydrocarbons and Alcohols. *ACS Nano* **2017**, *11*, 4825–4831.
8. Roldan Cuenya, B.; Behafarid, F., Nanocatalysis: Size- and Shape-Dependent Chemisorption and Catalytic Reactivity. *Surf. Sci. Rep.* **2015**, *70*, 135–187.
9. Jeon, H. S.; Kunze, S.; Scholten, F.; Roldan Cuenya, B., Prism-Shaped Cu Nanocatalysts for Electrochemical CO₂ Reduction to Ethylene. *ACS Catal.* **2018**, *8*, 531–535.
10. Schryer, D. R.; Upchurch, B. T.; Van Norman, J. D.; Brown, K. G.; Schryer, J., Effects of Pretreatment Conditions on a Pt/SnO₂ Catalyst for the Oxidation of CO in CO₂ Lasers. *J. Catal.* **1990**, *122*, 193–197.

11. Bamwenda, G. R.; Tsubota, S.; Nakamura, T.; Haruta, M., The Influence of the Preparation Methods on the Catalytic Activity of Platinum and Gold Supported on TiO₂ for CO oxidation. *Catal. Lett.* **1997**, *44*, 83–87.
12. Zhang, Z.; Yates, J. T., Band Bending in Semiconductors: Chemical and Physical Consequences at Surfaces and Interfaces. *Chem. Rev.* **2012**, *112*, 5520–5551.
13. Pitters, J. L.; Dogel, I. A.; Wolkow, R. A., Charge Control of Surface Dangling Bonds Using Nanoscale Schottky Contacts. *ACS Nano* **2011**, *5*, 1984–1989.
14. Shan, X.; Díez-Pérez, I.; Wang, L.; Wiktor, P.; Gu, Y.; Zhang, L.; Wang, W.; Lu, J.; Wang, S.; Gong, Q.; Li, J.; Tao, N., Imaging the Electrocatalytic Activity of Single Nanoparticles. *Nat. Nanotechnol.* **2012**, *7*, 668–672.
15. Caballero-Briones, F.; Artés, J. M.; Díez-Pérez, I.; Gorostiza, P.; Sanz, F., Direct Observation of the Valence Band Edge by *in Situ* ECSTM-ECTS in p-Type Cu₂O Layers Prepared by Copper Anodization. *J. Phys. Chem. C* **2009**, *113*, 1028–1036.
16. Choudhury, M. H.; Ciampi, S.; Yang, Y.; Tavallaie, R.; Zhu, Y.; Zarei, L.; Goncales, V. R.; Gooding, J. J., Connecting Electrodes with Light: One wire, Many Electrodes. *Chem. Sci.* **2015**, *6*, 6769–6776.
17. Choi, K.-S., Shape Control of Inorganic Materials *via* Electrodeposition. *Dalton Trans.* **2008**, 5432–5438.
18. Krämer, S.; Xie, H.; Gaff, J.; Williamson, J. R.; Tkachenko, A. G.; Nouri, N.; Feldheim, D. A.; Feldheim, D. L., Preparation of Protein Gradients through the Controlled Deposition of Protein–Nanoparticle Conjugates onto Functionalized Surfaces. *J. Am. Chem. Soc.* **2004**, *126*, 5388–5395.
19. Baker, B. E.; Kline, N. J.; Treado, P. J.; Natan, M. J., Solution-Based Assembly of Metal Surfaces by Combinatorial Methods. *J. Am. Chem. Soc.* **1996**, *118*, 8721–8722.
20. Bhat, R. R.; Fischer, D. A.; Genzer, J., Fabricating Planar Nanoparticle Assemblies with Number Density Gradients. *Langmuir* **2002**, *18*, 5640–5643.
21. Rajendra, R. B.; Jan, G.; Bryce, N. C.; Harry, W. S.; Andrea, L.-V., Controlling the assembly of nanoparticles using surface grafted molecular and macromolecular gradients. *Nanotechnology* **2003**, *14*, 1145.
22. Han, M.; Xu, C.; Zhu, D.; Yang, L.; Zhang, J.; Chen, Y.; Ding, K.; Song, F.; Wang, G., Controllable Synthesis of Two- Dimensional Metal Nanoparticle Arrays with Oriented Size and Number Density Gradients. *Adv. Mater.* **2007**, *19*, 2979–2983.
23. Lundgren, A.; Munktel, S.; Lacey, M.; Berglin, M.; Björefors, F., Formation of Gold Nanoparticle Size and Density Gradients *via* Bipolar Electrochemistry. *ChemElectroChem* **2016**, *3*, 378–382.
24. Longbing, H.; Xi, C.; Yuewen, M.; Fengqi, S.; Min, H., Two-Dimensional Gradient Ag Nanoparticle Assemblies: Multiscale Fabrication and SERS Applications. *Nanotechnology* **2010**, *21*, 495601.
25. Atsushi, Y.; Yoshihiko, S.; Takahiro, T.; Yoshiyuki, S., p-Cu₂O/SiC_xO_y/n-SiC/n-Si Memory Diode Having Resistive Nonvolatile Memory and Rectifying Behaviors. *Appl. Phys. Express* **2014**, *7*, 074203.
26. Tan, C.-S.; Chen, H.-S.; Chiu, C.-Y.; Wu, S.-C.; Chen, L.-J.; Huang, M. H., Facet-Dependent Electrical Conductivity Properties of PbS Nanocrystals. *Chem. Mater.* **2016**, *28*, 1574–1580.
27. Tan, C.; Shan; Chen, Y.; Jui; Hsia, C.; Fu; Huang, M. H., Facet Dependent Electrical Conductivity Properties of Silver Oxide Crystals. *Chem. - Asian J.* **2017**, *12*, 293–297.
28. Tan, C. S.; Hsieh, P. L.; Chen, L. J.; Huang, M., H., Silicon Wafers with Facet-Dependent Electrical Conductivity Properties. *Angew. Chem., Int. Ed.* **2017**, *56*, 15339–15343.
29. Su, Y.; Li, H.; Ma, H.; Robertson, J.; Nathan, A., Controlling Surface Termination and Facet Orientation in Cu₂O Nanoparticles for High Photocatalytic Activity: A Combined

- Experimental and Density Functional Theory Study. *ACS Appl. Mater. Interfaces* **2017**, *9*, 8100–8106.
30. Vogel, Y. B.; Zhang, L.; Darwish, N.; Gonçalves, V. R.; Le Brun, A.; Gooding, J. J.; Molina, A.; Wallace, G. G.; Coote, M. L.; Gonzalez, J.; Ciampi, S., Reproducible flaws unveil electrostatic aspects of semiconductor electrochemistry. *Nat. Commun.* **2017**, *8*, 2066.
 31. Yang, Y.; Ciampi, S.; Gooding, J. J., Coupled Thermodynamic and Kinetic Changes in the Electrochemistry of Ferrocenyl Monolayers Induced by Light. *Langmuir* **2017**, *33*, 2497–2503.
 32. Gunawardena, G.; Hills, G.; Montenegro, I.; Scharifker, B., Electrochemical nucleation: Part I. General considerations. *J. Electroanal. Chem.* **1982**, *138*, 225–239.
 33. Soon, A.; Todorova, M.; Delley, B.; Stampfl, C., Thermodynamic Stability and Structure of Copper Oxide Surfaces: A first-Principles Investigation. *Phys. Rev. B* **2007**, *75*, 125420.
 34. Suleiman, I. A.; Radny, M. W.; Gladys, M. J.; Smith, P. V.; Mackie, J. C.; Kennedy, E. M.; Dlugogorski, B. Z., Chlorination of the Cu(110) Surface and Copper Nanoparticles: A Density Functional Theory Study. *J. Phys. Chem. C* **2011**, *115*, 13412–13419.
 35. Bonnet, N.; Marzari, N., First-Principles Prediction of the Equilibrium Shape of Nanoparticles Under Realistic Electrochemical Conditions. *Phys. Rev. Lett.* **2013**, *110*, 086104.
 36. Carlson, D. E.; Rajan, K., Irreversible Light-Enhanced Degradation in Amorphous Silicon Solar Cells at Elevated Temperatures. *Appl. Phys. Lett.* **1996**, *68*, 28–30.
 37. Kraya, R.; Kraya, L. Y.; Bonnell, D. A., Orientation Controlled Schottky Barrier Formation at Au Nanoparticle–SrTiO₃ Interfaces. *Nano Lett.* **2010**, *10*, 1224–1228.
 38. Shaik, S.; Mandal, D.; Ramanan, R., Oriented Electric Fields as Future Smart Reagents in Chemistry. *Nat. Chem.* **2016**, *8*, 1091–1098.
 39. Ferreira, P. J.; Shao-Horn, Y., Formation Mechanism of Pt Single-Crystal Nanoparticles in Proton Exchange Membrane Fuel Cells. *Electrochem. Solid-State Lett.* **2007**, *10*, B60–B63.
 40. Sinitskii, A.; Dimiev, A.; Corley, D. A.; Fursina, A. A.; Kosynkin, D. V.; Tour, J. M., Kinetics of Diazonium Functionalization of Chemically Converted Graphene Nanoribbons. *ACS Nano* **2010**, *4*, 1949–1954.
 41. Azzaroni, O.; Vela, M. E.; Fonticelli, M.; Benítez, G.; Carro, P.; Blum, B.; Salvarezza, R. C., Electrodesorption Potentials of Self-Assembled Alkanethiolate Monolayers on Copper Electrodes. An Experimental and Theoretical Study. *J. Phys. Chem. B* **2003**, *107*, 13446–13454.
 42. Zhang, L.; Vogel, Y. B.; Noble, B. B.; Gonçalves, V. R.; Darwish, N.; Brun, A. L.; Gooding, J. J.; Wallace, G. G.; Coote, M. L.; Ciampi, S., TEMPO Monolayers on Si(100) Electrodes: Electrostatic Effects by the Electrolyte and Semiconductor Space-Charge on the Electroactivity of a Persistent Radical. *J. Am. Chem. Soc.* **2016**, *138*, 9611–9619.
 43. Vogel, Y. B.; Gonçalves, V. R.; Gooding, J. J.; Ciampi, S., Electrochemical Microscopy Based on Spatial Light Modulators: A Projection System to Spatially Address Electrochemical Reactions at Semiconductors. *J. Electrochem. Soc.* **2018**, *165*, H3085–H3092.

Table of Content (TOC) graphics

One nanoparticle, many diodes

